



ELSEVIER

Available online at [www.sciencedirect.com](http://www.sciencedirect.com)

SCIENCE @ DIRECT®

Surface Science 537 (2003) 95–112



[www.elsevier.com/locate/susc](http://www.elsevier.com/locate/susc)

# Electrochemical growth of gold on well-defined vicinal H–Si(1 1 1) surfaces studied by AFM and XRD

M.L. Munford<sup>a,b</sup>, F. Maroun<sup>a,1</sup>, R. Cortès<sup>a,1</sup>, P. Allongue<sup>a,\*,1</sup>, A.A. Pasa<sup>b</sup>

<sup>a</sup> *Laboratoire de Physique des Liquides et Electrochimie (CNRS UPR-15), Université P & M Curie, 4 Place Jussieu, F-75005 Paris, France*

<sup>b</sup> *Laboratorio de Filmes Finos e Superfícies, Departamento de Física, UFSC, 88040-900 Florianópolis, SC, Brazil*

Received 8 January 2003; accepted for publication 8 April 2003

## Abstract

The possibility of preparing structurally well-defined and periodically arranged metal islands on a semiconductor is very attractive for optical and magnetic applications. In this work we used electrochemical deposition to grow nm-sized gold islands that decorate steps on defect-free vicinal H terminated Si(1 1 1) surfaces prepared by chemical etching. The gold deposits were studied by atomic force microscopy and X-ray diffraction. Results show that gold nucleates exclusively along the steps and that the density of nuclei is controlled by the electrode potential. Nearly perfect replication of the periodic array of straight monatomic steps is achieved at sufficiently negative potential. XRD indicates that the structure of gold films evolves from powder-like, close to the onset potential of nucleation (–1.6 V), to strongly epitaxial with the (1 1 1) orientation at more negative potentials. A reaction model and a growth mechanism are proposed to account for the origin of the selective nucleation and the excellent epitaxy obtained. In particular they discuss whether or not the H-monolayer remains intact under the deposit.

© 2003 Elsevier Science B.V. All rights reserved.

**Keywords:** Silicon; Gold; Electrochemical methods; Epitaxy; Growth; Atomic force microscopy; X-ray scattering, diffraction, and reflection

## 1. Introduction

The preparation of well-defined and periodically arranged metal islands on a semiconductor is very attractive for optical and magnetic applications. Most recent works considered metal evaporation

on pre-structured  $7 \times 7$ -Si(1 1 1) clean surfaces [1] and on vicinal  $7 \times 7$ -Si(1 1 1) surfaces that were functionalized by pre-depositing gold and  $\text{CaF}_2$  [2,3]. Metal deposition on silicon is such an important technological step that it prompted numerous studies on *clean* silicon surfaces and on H-terminated silicon surfaces [4], especially after the work of Chabal and co-workers [5] who established that H–Si surfaces are technologically relevant and stable in air. The comparison of metal evaporation on the two types of silicon surfaces shows that the presence of the H-monolayer is sufficient to promote drastic changes in the growth modes, from a

\* Corresponding author. Tel.: +1-6933-4431; fax: +1-6933-3004.

E-mail address: [pa@pmc.polytechnique.fr](mailto:pa@pmc.polytechnique.fr) (P. Allongue).

<sup>1</sup> Permanent address: CNRS—UMR 7643, Ecole Polytechnique Lab., Physique de la Matière Condensée, F-91128 Palaiseau, France.

layer-by-layer process onto clean silicon to a Volmer–Weber mechanism on the H-terminated surface (for a review see [4]). Epitaxy of the metal film on H–Si(1 1 1) was reported in few cases such as Ag and Au for instance. A key issue, often debated, concerns the eventual segregation (or removal) of the hydrogen layer under the deposit [4].

Metal deposition on H-terminated silicon was also performed using electrochemical growth. The method constitutes an alternative method, which is widely used in microelectronics because it is cost effective and allows fast growth rates. The growth modes are also simply modified by changing the applied potential and the solution composition. Recent studies of this kind concerned the deposition of copper [6–9], lead [7,10–12], gold [13–15], magnetic layers Co–Ni–Cu/Cu [16,17], cobalt [18,19] and nickel [20] on Si(1 1 1) or (1 0 0). Iron was also deposited on porous silicon [21]. Metal plating was also performed without applying an external bias (electroless deposition) from fluoride-based solutions. The electroless deposition of Cu/Si(1 1 1) [22], Au/Si(1 1 1) [7,23], Pt and Ni [24,25] has in particular been investigated. These electrochemical studies often focused on one specific point of the film formation such as the growth modes using current transient measurements or STM/AFM observations. In some studies the structure of the deposits was studied by X-ray techniques. Very few works combined different techniques and, to the best of our knowledge, none succeeded in controlling the spatial arrangement of the metallic nanostructures on the silicon surface.

This work shows for the first time that it is possible to prepare well defined and periodically arranged arrays of gold nm-islands by template electrodeposition on a defect free vicinal H-terminated Si(1 1 1) surface. The substrates, with a stepped structure close to perfection, were obtained by controlled chemical etching [26] and the ultrathin gold layers (1–20 ML) were electrodeposited from an alkaline  $\text{KAu}(\text{CN})_2$  solution. The gold films were characterized in details by ex-situ AFM, X-ray diffraction (XRD) and electrochemical transient techniques. Results reveal a strong potential-dependence of the film morphology and structure. The *long-range* replication

of the stepped surface structure is achieved, under optimum conditions of polarization, by highly selective nucleation of a large density of gold clusters at the silicon step edges. Subsequent growth is 3D. A reaction model and a growth mechanism are proposed to account for observations. They address, in particular, whether or not the H-monolayer remains intact under the deposit.

## 2. Experimental

### 2.1. Substrate preparation

Silicon samples were cut from 1 to 10  $\Omega\text{cm}$  (1 1 1) wafers (n-type, P doped) with a miscut angle  $\alpha = 0.2^\circ$ ,  $0.4^\circ$  or  $2^\circ$  precisely oriented towards  $\langle 1 1 -2 \rangle$ . They will be referred to as Si- $0.2^\circ$ , Si- $0.4^\circ$  and Si- $2^\circ$  in the following. The careful adjustment of the miscut orientation is a prerequisite to obtain straight and parallel monatomic steps (Fig. 1a) terminated by monohydride sites (Fig. 1b) [26]. The step-to-step distance of  $W \sim 140$  nm measured in Fig. 1a corresponds to a misorientation  $0.13^\circ$ , which is very close to the miscut angle derived from XRD on this substrate ( $\tan(\alpha) = W(\text{nm})/h$ , where  $h = 0.314$  nm is the height of a step) [26]. Prior to etching, samples were cleaned in (98%  $\text{H}_2\text{SO}_4$ )/(30%  $\text{H}_2\text{O}_2$ ) 2:1 mixture and rinsed with bidistilled water. The H-termination was obtained by chemical etching in oxygen-free 40%  $\text{NH}_4\text{F}$  [27–29] to avoid the formation of triangular etch pits on the (1 1 1) terraces. We used 50 mM  $(\text{NH}_4)_2\text{SO}_3$  as oxygen scavenger [26,28]. A final rinse in bidistilled water was performed after etching. Prior to use the ohmic contact was formed by applying an InGa eutectic on the rear face. The sample was then mounted with its lateral edges protected by an electrolytic scotch tape to expose only the well-defined (1 1 1) face to solution.

### 2.2. Gold deposition on Si(1 1 1)

Gold was deposited from 5 mM  $\text{KAu}(\text{CN})_2$  + 10 mM NaCN in 2 M NaOH, using a three-electrode electrochemical cell connected to a potentiostat

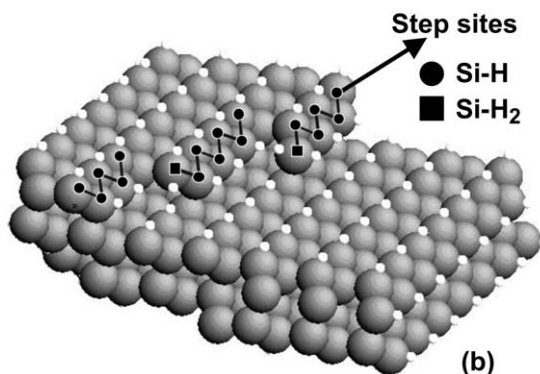
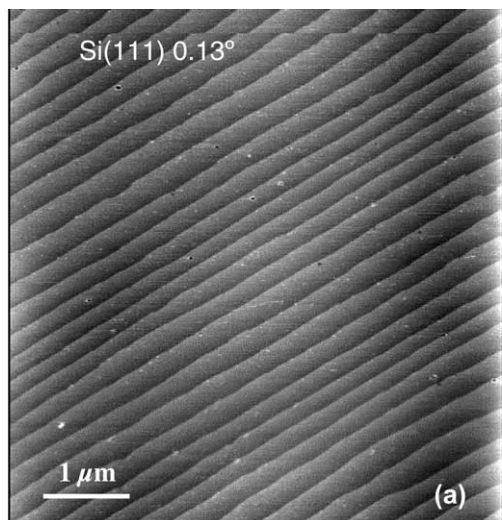


Fig. 1. (a) AFM image ( $5\ \mu\text{m} \times 5\ \mu\text{m}$ ) of a H-Si(111) surface with  $0.13^\circ$  miscut angle. (b) Ball model of the Si(111) surface with two terraces separated by one step containing two kink sites. Other sites are monohydride sites. Dark and white spheres are Si and H atoms. The zigzagging line indicates the step sites.

(Ecochemie, The Netherlands). The reference electrode was a mercury sulfate electrode (MSE) and all potentials are quoted against this reference of potential. The counter electrode was a Pt grid. The procedure for deposition was as follows: immediately after etching the sample was quickly mounted (see above) and manually immersed into the solution at the desired pre-set deposition potential to avoid any chemical etching. After deposition, the sample was quickly removed from the solution, rinsed with bidistilled water, and blown dried with nitrogen.

### 2.3. Atomic force microscopy

The morphology of the gold deposits was characterized by contact mode atomic force microscopy, AFM (Molecular Imaging microscope, Phoenix, USA) in a nitrogen atmosphere.  $\text{Si}_3\text{N}_4$  cantilevers (Nanoprobes, spring constant  $0.12\ \text{Nm}^{-1}$ ) were used. In general, stable imaging was obtained, except when the deposition potential was too close to the onset of nucleation ( $U \sim -1.6\ \text{V}$ ). In that case, the Au clusters were wiped by the AFM tip.

### 2.4. X-ray diffraction

A home-built five-circle diffractometer was used with a  $\text{K}\alpha_1$  Cu source ( $\lambda = 1.5405\ \text{\AA}$ ). The sample configuration is presented in Fig. 2. The X-ray beam is horizontal and parallel to  $XX'$ . Before measurements, the sample optical plane was carefully adjusted to bring the normal  $n$  parallel to the rotation axis  $ZZ'$  by minimizing the deflection of a laser beam upon in-plane rotation of the sample. To diffract on Au(111) planes parallel to the surface,  $\theta$ -scans were performed by varying the sample angle  $\theta$  around the diffraction angles  $\theta_{\text{Si}(111)}$  or  $\theta_{\text{Au}(111)}$  with the detector positioned for Bragg conditions ( $h = 2\theta_{\text{Si}(111)}$  or  $2\theta_{\text{Au}(111)}$ ). For grazing incidence measurements or  $\Phi$ -scans, the sample angle was  $\theta = 0.6^\circ$  and the detector positioned in Bragg conditions for  $\{11-1\}$  planes of gold or silicon. The settings ( $h$ , AZ) for the two types of experiments are given in Table 1. For a quantitative comparison of different deposits the XRD spectra were normalized with respect to the intensity of the Si(11-1) peak.

### 2.5. Rutherford backscattering (RBS) measurements

The film thickness was determined from RBS measurements, using the 2 MeV van de Graaf accelerator at the Groupe de Physique des Solides (Université Paris 7). The surface density of Au atoms was converted into an average thickness expressed in ML, with  $1\ \text{ML} = 1.38 \times 10^{15}\ \text{atoms}/\text{cm}^2$ . The film thickness was also derived from

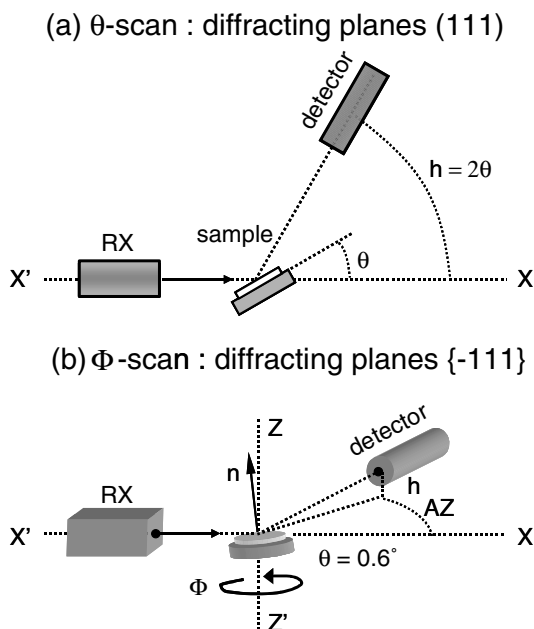


Fig. 2. Definition of angles in XRD experiments. (a)  $\theta$ -scans: the detector is positioned at  $h = 2\theta_{\text{Au}(111)}$  ( $AZ = 0$ ) to diffract on Au(111) planes and the sample angle varied around  $\theta_{\text{Au}(111)}$ ; (b)  $\Phi$ -scans: the sample plane is carefully adjusted to bring the surface normal  $n$  parallel to the rotation axis  $ZZ'$ . The angle  $\Phi$  is varied with the sample normal  $n$  tilted by  $0.6^\circ$  and the detector position set at  $h$  and  $AZ$  to diffract on Au{11-1} planes.

Table 1  
Experimental conditions used in X-ray characterizations

Experiment	Planes	$\theta$	$AZ$	$h$
$\theta$ -scan	Si(111)	14.221	0	28.443
	Au(111)	19.087	0	38.173
$\Phi$ -scan	Si(111)	0.6	26.9	9.35
	Au(111)	0.6	36.38	12.46

See Fig. 2 for the definition of parameters.

integration of the deposition current (using Faraday's law).

### 3. Results

#### 3.1. Deposition procedure

The voltammograms of an n-type H-Si(111) electrode in the presence and absence of  $\text{KAu}(\text{CN})_2$  are shown in Fig. 3. The current was

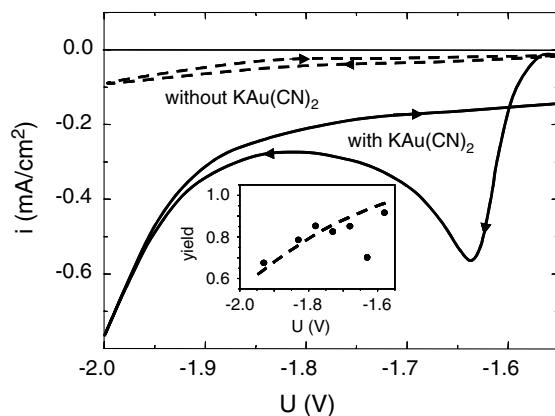


Fig. 3. Voltammograms of a n-type H-Si(111) in 2 M NaOH + 10 mM NaCN, in the presence (—) and in the absence (---) of  $\text{KAu}(\text{CN})_2$ . The sweep rate is 15 mV/s. Inset: variations of the deposition yield as a function of the deposition potential. Data correspond to 7 s deposits at each potential.

very small for  $U > -1.5$  V (not shown) due to the rectifying behavior of the interface n-Si/solution. Direct polarization regime or accumulation of electrons corresponds to  $U < -1.5$  V, which is slightly negative of the free potential of the surface in this solution.<sup>2</sup> In the blank solution (no  $\text{KAu}(\text{CN})_2$  added, dotted line), the small cathodic current indicates that the kinetics of water decomposition is very slow on H-Si(111). In the gold solution (solid line), the sharp rise of the current at  $-1.57$  V corresponds to the nucleation onset of gold deposition. The presence of a peak of current at  $-1.65$  V indicates that deposition becomes limited by mass transport of  $\text{Au}(\text{CN})_2^-$  species in solution. For  $U < -1.9$  V, the decomposition of water becomes significant on the gold deposit. The return scan, which corresponds to gold on gold deposition, indicates that the growth of gold on gold is easier than the nucleation of gold on H-Si(111) since the current is not zero for  $U > -1.57$  V.

The deposition was performed by immersing the sample under potential control. The conditions will be defined in the following, either by the ap-

<sup>2</sup> The region of potentials  $U > -1.5$  V was not explored to avoid the passivation of the surface.

plied potential  $U$  quoted against the reference electrode or by the overpotential  $\eta = U - U_0 > 0$ , with  $U_0 = -0.82$  V is the Nernst potential of the reaction  $\text{Au}(\text{CN})_2^- + e^- \rightarrow \text{Au}$  ( $U_0$  was measured as the rest potential of a gold wire in an oxygen-free gold solution). The yield of deposition was determined by dividing the gold thickness derived from RBS by the gold thickness derived from Faraday's law using the conversion factor  $1 \text{ ML} = 220 \mu\text{C}/\text{cm}^2$  (one electrons is exchanged per deposited gold atom). The curve in inset of Fig. 3 shows that the deposition yield decreases continuously from unity, close to the nucleation onset ( $-1.57$  V), to 0.6 at  $-1.93$  V. The results of Fig. 3 were not significantly depending on the miscut angle of the substrate.

The transient electrochemical current  $i(t)$  monitored during deposition is shown in Fig. 4a and b for two potentials. Solid and dashed lines correspond to Si- $2^\circ$  and  $0.2^\circ$ . Two peaks are observed. The narrow one ( $t < 0.1$  s) corresponds to the immersion of the sample under potential control. A broader peak occurs after some delay. This peak

is related to the nucleation and growth modes and was characterized by its maximum (absolute value)  $i = i_{\text{max}}$  at  $t = t_{\text{max}}$ . For a given miscut,  $i_{\text{max}}$  increases and  $t_{\text{max}}$  decreases with increasing  $\eta$ . At a given potential,  $i_{\text{max}}$  increases and  $t_{\text{max}}$  decreases with increasing miscut. Using  $i_{\text{max}}$  and  $t_{\text{max}}$ , the dimensionless transients  $(i/i_{\text{max}})^2$  vs.  $(t - t_0)/(t - t_0)_{\text{max}}$  were plotted (see the review of Oskam and Searson [14] for more details) to identify the nature of the nucleation and growth process. The time  $t_0$  represents an induction time corresponding to the delay of current rise. Fig. 4c shows that  $t_0$  decreases with increasing  $\eta$  and that there is no significant influence of the step density. In Fig. 4d all the dimensionless transients measured at different potentials on Si- $0.2^\circ$  merge into one single plot (symbols), which fits very well with the hypothesis of a progressive (solid curve) and not with an instantaneous (dotted line) nucleation process (the expression of model curves is given in [13]). The same result is obtained with the Si- $0.4^\circ$  and Si- $2^\circ$  substrates.

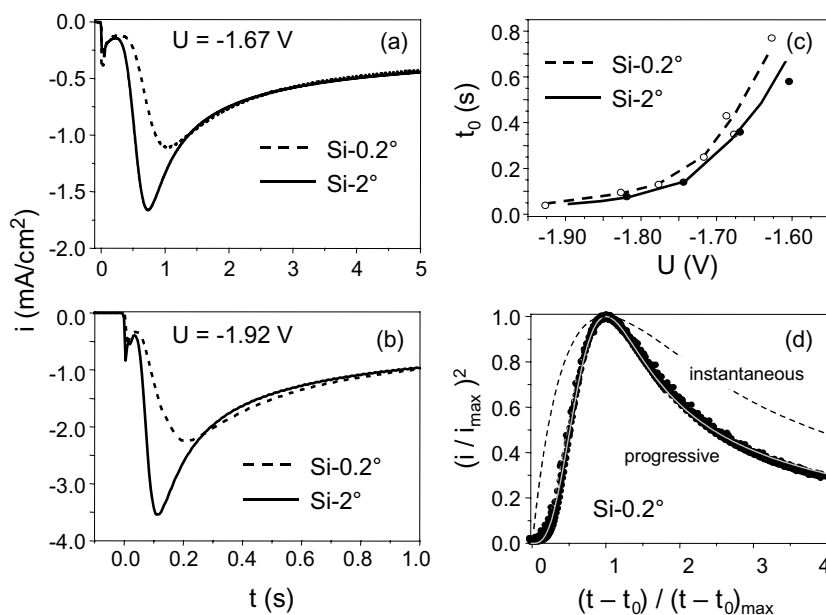


Fig. 4. (a and b) Current transients for  $U = -1.67$  and  $-1.9$  V recorded in the same solution as in Fig. 3. Solid and dotted lines correspond to Si- $2^\circ$  and Si- $0.2^\circ$  substrates. (c) Potential dependence of the induction time  $t_0$ . (d) Dimensionless transients for the substrate Si- $0.2^\circ$ . See text for explanation. Solid and dashed lines are model curves corresponding to progressive and instantaneous nucleation [13].

### 3.2. AFM observations

In this section we will show that gold deposition follows a Volmer–Weber mechanism with the formation of 3D clusters that exclusively decorate the silicon steps for  $U = -1.93 \text{ V} < U < -1.60 \text{ V}$ . The location, density and morphology of the gold clusters were studied as a function of the potential, deposition time and step density.

Fig. 5 shows AFM images of 5.2, 7.2 and 18.4 ML-thick gold films deposited on Si-0.2° at  $U = -1.73 \text{ V}$ . The films consist in nm-sized clusters which are aligned along parallel lines separated, on average, by 90, 115 and 100 nm, respectively in images (a–c). These distances are close to the nominal terrace width on this substrate ( $W \sim 90 \text{ nm}$  for 0.2°). The image contrast was enhanced in Fig. 5d to resolve the silicon steps and

confirm that the steps are indeed running from top to bottom in the images and demonstrate that the gold clusters are precisely located on them. In Fig. 5a–c the island density is nearly independent of time ( $\sim 1.3 \times 10^{10} \text{ cm}^{-2}$ ) and their average height increases from 19 nm (approximately 80 ML) to 27 nm (114 ML) while their width increases from 47 to 90 nm at FWHM. The islands present therefore an aspect ratio height/width  $\sim 0.4$ . At the end of the growth some of the islands take a well-defined geometric shape (e.g. see flat top triangles in Fig. 5c). This point will be further discussed below.

Two 9–10-ML thick gold deposits grown at  $-1.92 \text{ V}$  on Si-0.2° and Si-0.4° are shown in Fig. 6. The gold islands are again distributed along the steps. Comparing Fig. 6a with Fig. 5c reveals that changing the deposition potential from  $-1.73 \text{ V}$  to  $-1.92 \text{ V}$  increases the island density by a factor 2

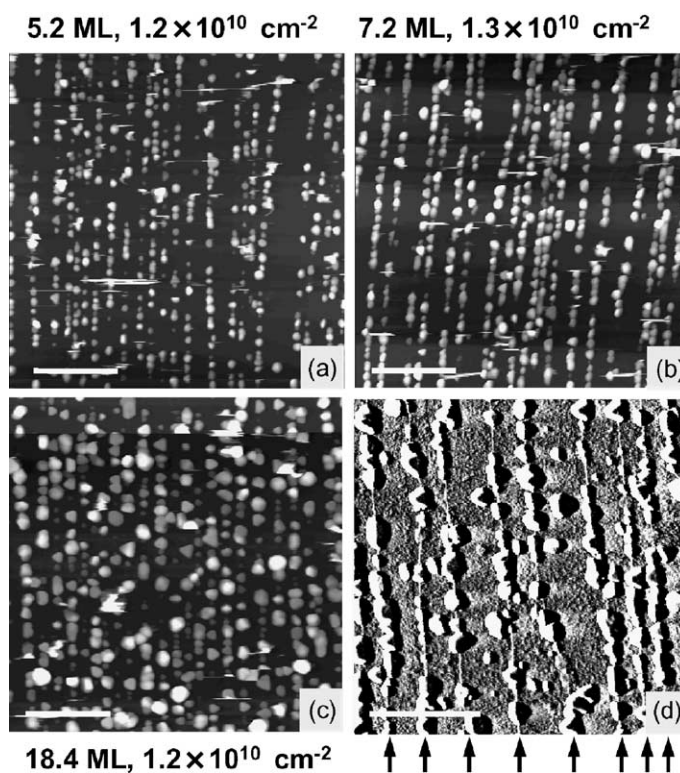


Fig. 5. AFM images of gold deposits on Si-0.2° ( $U = -1.73 \text{ V}$ ). The thickness is respectively 5.2 ML (a), 7.2 ML (b) and 18.4 ML (c). Images are  $(2 \mu\text{m} \times 2 \mu\text{m})$ . In (d) the image contrast is enhanced to show that the gold islands are located at steps ( $1.5 \mu\text{m} \times 1.5 \mu\text{m}$  image). In all images the steps are running vertically from top to bottom in images and are descending from right to left. Their position is identified by arrows in (d). The bar is 500 nm for all images.

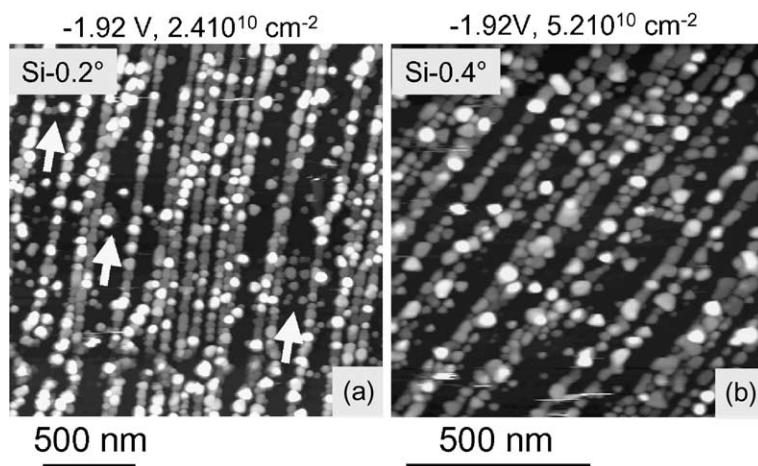


Fig. 6. AFM images of 9–10 ML-thick gold deposits on Si-0.2° (a) and Si-0.4° (b). The deposition potential is  $U = -1.92$  V in both cases. The silicon steps are running vertically in (a) and oblique in (b). Note that only few Au islands have nucleated on (111) terraces (see arrows in a) and that the density of islands along the steps is nearly the same in both images.

and that this increase merely corresponds to an increase of the *linear* island density along the steps, from  $10^5$  to  $2 \times 10^5$  clusters/cm, because only very few islands have nucleated on the (111) terraces at  $-1.92$  V (arrows in Fig. 6a). Increasing the overpotential reduces both the size and the size dispersion of clusters. At  $U = -1.92$  V the average height is only 12 nm and the lateral size 55 nm. On Si-0.4° the island density is  $5.2 \times 10^{10}$  cm $^{-2}$  at the same potential of  $-1.92$  V (Fig. 6b), which is twice as large as on Si-0.2° (Fig. 6a). The factor 2 scales exactly with the doubled step density on Si-0.4° and means that there are also  $2.5 \times 10^5$  islands/cm along the steps.

Fig. 7 presents the height derivative of the topography of a deposit performed at  $U = -1.73$  V during 5 s. The islands appear as well defined flat top polyhedrons with adjacent edges separated by an angle of 60° or 120°. Triangles (marked by triangles) and trapezes (marked with trapezes) are the most frequently encountered shapes. Hexagonal islands are more scarcely observed. A careful analysis of the islands shows that their edges are parallel to the preferential directions shown in inset of image 7a. These directions are 60° apart (sixfold symmetry) and one of the direction is parallel to  $\langle 1-10 \rangle$  or, equivalently, to the step direction. A close examination of the triangular

islands in Fig. 7a shows that there are two types of islands. Triangles of type (A) and (B) which are respectively pointing to the right and the left of the image. Zooming inside the rectangular boxes (Fig. 7b–c) evidences that triangles of type (A) and (B) are overlapping preferentially with the upper terrace and the bottom terrace (see also scheme).

### 3.3. X-ray diffraction measurements

A  $\theta$ -scan close to the Bragg conditions for Si(111) planes parallel to the surface (not shown) gives a peak at the expected angle  $\theta_{\text{Si}(111)} = 14.22^\circ$  (Table 1). A  $\Phi$ -scan (not shown) with the detector in Bragg position for Si{11-1} planes exhibits three peaks at 104.89°, 224.89° and 344.89° corresponding to (11-1), (1-11) and (-111) diffracting planes. After gold deposition a diffraction peak is found in  $\theta$ -scans at the expected value  $\theta_{\text{Au}(111)} = 19.09^\circ$  for Au(111) planes parallel to the surface (Table 1), meaning that the deposit presents a (111) texture. In  $\Phi$ -scans with the detector in Bragg position for Au{11-1} planes (Table 1) 6 peaks are observed: three of them (110.07°, 230.07° and 350.07°) are close to the peak position of silicon and will be referred to as ‘even peaks’ in the following. The other three peaks, shifted by 60°, will be referred to as ‘odd

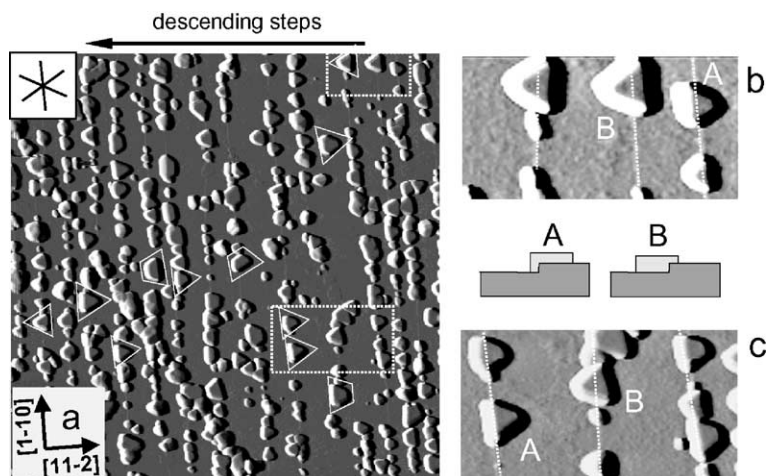


Fig. 7. (a) Height derivative AFM image ( $2\ \mu\text{m} \times 2\ \mu\text{m}$ ) of a gold deposit on H-Si(1 1 1)-0.2° ( $U = -1.73\ \text{V}$ , 5 s). Triangles and trapezes outline triangular and trapezoidal islands. The sixfold orientations taken by the edges of polyhedron islands are given in inset. (b) and (c) Zoom corresponding to rectangular boxes in (a) to evidence the two sorts of triangular islands. The dotted lines mark the step position. The islands of type (A) and (B) overlap preferentially with the upper and the bottom terrace respectively (see also schematic cross section).

peaks'. The sixfold symmetry of  $\Phi$ -scans indicates that the deposit is in epitaxy with the surface. The even peaks correspond to the relationship of epitaxy Au(1 1 1)[1 -1 0]||Si(1 1 1)[1 -1 0] (with respect to bulk axis of silicon) and the odd ones to gold clusters that are rotated by 180°.

As a preliminary remark it should be noted that the linewidth of XRD peaks is not limited by the grain size. According to the Scherer formula, the broadening (in degrees) of the linewidth is  $\sim(\pi/180)\lambda/(L * \cos(\theta))$  where  $L$  is the dimension of the grain in the diffraction plane and  $\lambda = 1.54\ \text{\AA}$  the X-ray wavelength. In the case of  $\theta$ -scans,  $L$  is equal to the height of clusters. In the case of  $\Phi$ -scans, the {1 1 -1} diffracting planes are tilted by 57° and  $L \sim 1.2 \times \text{height}$  because the aspect ratio of grains is smaller than unity. Hence, for most deposits studied here the peak linewidth of XRD spectra reflects the film structure since the Scherer broadening remains  $<0.4^\circ$  for islands thicker than 20 nm.

In the following two paragraphs we study the evolution of  $\theta$ - and  $\Phi$ -scans as a function of the metal thickness (at constant deposition potential) and as a function of the deposition potential (at constant thickness). The influence of the step di-

rection on  $\theta$ -scans is investigated in a later paragraph.

### 3.4. Thickness dependence of $\theta$ - and $\Phi$ -scans

Fig. 8 shows the  $\theta$ -scans of the gold deposits imaged in Fig. 5 ( $U = -1.73\ \text{V}$ , Si-0.2°). All scans were recorded with  $\Phi = 90^\circ$ , i.e. with the X-ray beam *parallel* to steps. The gold thickness  $t_{\text{Au}}$  ranges from 5.2 to 18.4 ML as indicated in the figure. The strong increase of the peak intensity with growth (Fig. 8a), scales linearly with  $t_{\text{Au}}$  in Fig. 8b, with the intercept of the plot passing through the origin. More remarkable is the corresponding narrowing of the peak linewidth from 2° to 1°. The  $\Phi$ -scans of the same deposits are given in Fig. 9. They exhibit 6 peaks, as explained above, which intensity increases linearly with the gold thickness (not shown). A quantitative analysis of the spectra (Fig. 9b) evidences a significant improvement of the film mosaicity with  $t_{\text{Au}}$  because the peak linewidth decreases from 6.6° to 4.5°. Fig. 9b plots also the ratio  $R$  of the integrated intensity of the 6 peaks (after background correction) to the total integrated signal.  $R$  gives the proportion of the deposit which is in epitaxy with

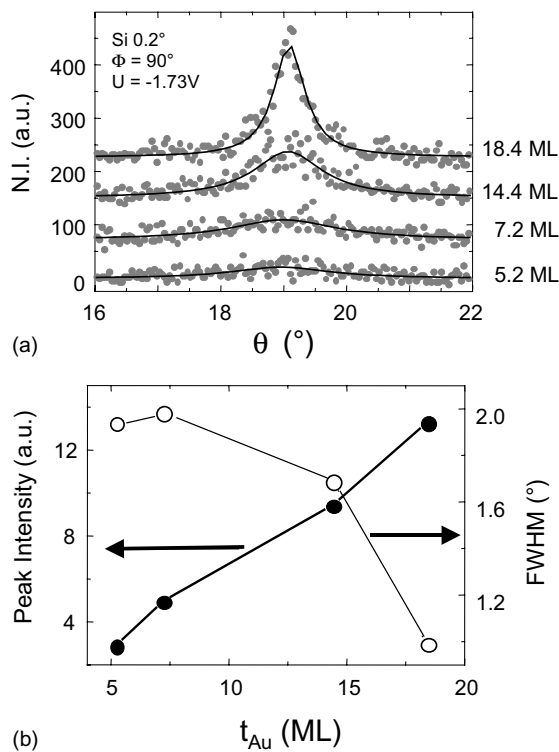


Fig. 8. (a)  $\theta$ -scans around  $\theta_{\text{Au}(111)}$  for gold deposits on Si-0.2° ( $U = -1.73$  V).  $t_{\text{Au}}$  is indicated in ML in the figure. Solid lines are Lorentzian fits. (b) Variations of the peak intensity and FWHM as a function of gold thickness.

the Si(111) surface:  $R = 0$  corresponds to a powder-like structure (no preferential orientation of the grains) and  $R = 1$  means perfect epitaxy. Experimentally,  $R$  increases approximately linearly with  $t_{\text{Au}}$  (Fig. 9b).

### 3.5. Influence of the deposition potential

The influence of the deposition potential on  $\theta$ - and  $\Phi$ -scans is shown in Fig. 10 for films of thickness  $t_{\text{Au}} = 10 \pm 1$  ML. There is a remarkable increase, in both types of scans, of the peak intensity with increasing  $\eta$ . There is also a systematic evolution of the peak linewidth. In  $\Phi$ -scans the FWHM decreases with increasing  $\eta$  while it increases in  $\theta$ -scans measured with  $\Phi = 0^\circ$  (i.e. with the beam perpendicular to the step direction). This last point is commented below. Fig. 11 details the potential dependence of the  $\Phi$ -scans. The sets of

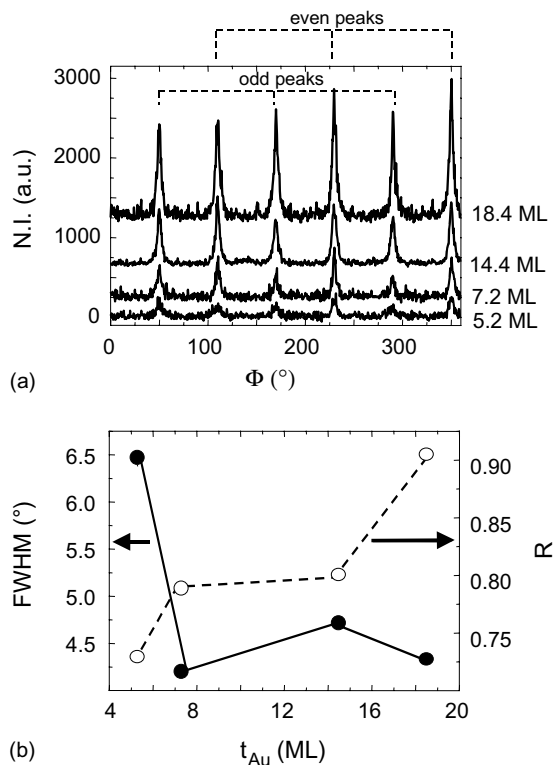


Fig. 9. (a)  $\Phi$ -scans corresponding to the  $\theta$ -scans of Fig. 8. The film thickness is indicated in the figure. (b) Quantitative analysis of spectra. Variations of the peak linewidth and  $R$  with the metal thickness. See text for the definition of  $R$ . Note the sixfold symmetry of spectra.

data points shown in each graph correspond to deposits of similar thickness on substrates with different miscut angles. The same symbols are used in the four graphs. For a given step density, the different plots show clear trends for  $-1.93$  V  $< U < -1.6$  V. Fig. 11a shows that the normalized intensity increases by a factor 4. The peak linewidth decreases from 6–7° to 2° (Fig. 11b) and  $R$  increases rather abruptly from 0.6, close to the onset of nucleation ( $U \sim -1.6$  V), to 0.9 for  $U < -1.68$  V (Fig. 11c). The last parameter derived from the analysis of  $\Phi$ -scan is  $R'$  the ratio of the integrated intensity of the odd peaks divided by the intensity of the even peaks (after background correction).  $R'$  gives the proportion of the (111) gold islands which are rotated by 180° with respect to the axis of bulk silicon. Fig. 11d shows

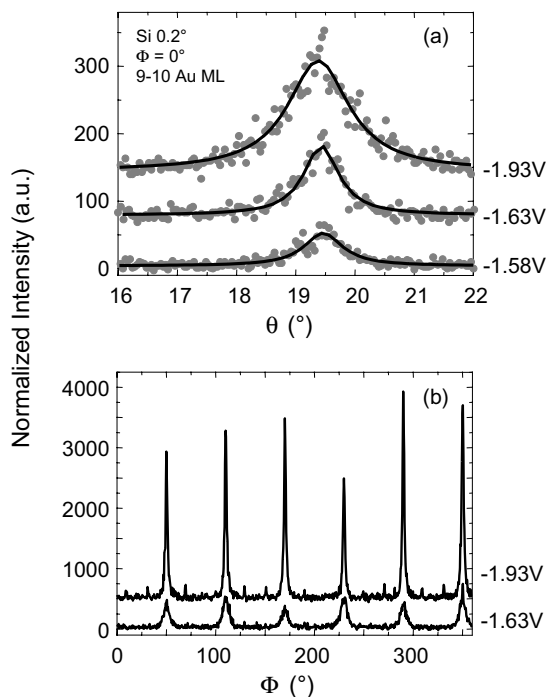


Fig. 10. Series of  $\theta$ - and  $\Phi$ -scans showing the influence of the deposition potential (indicated in the figure) on the film structure. Note the increase of the peak intensity, in both kinds of scans, with decreasing deposition potentials.

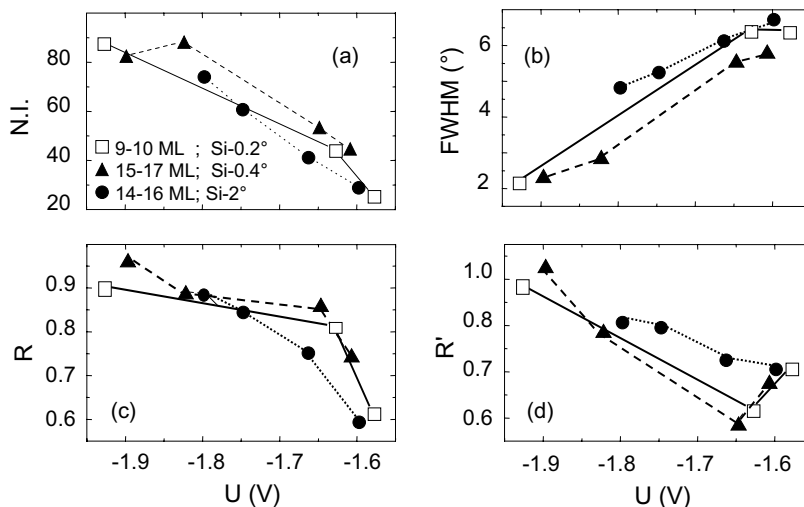


Fig. 11. Quantitative analysis of  $\Phi$ -scans as a function of the deposition potential. For each substrate only deposits of similar thickness are compared. Triangles, circles and squares respectively correspond to 14–16 ML films on Si-2°, 15–17 ML films on Si-0.4° and 9–10 ML films on Si-0.2° in all graphs. (a) Total normalized intensity integrated under the six peaks. (b) Average peak linewidth. (c and d) variations of  $R$  and  $R'$ . See text for the definition of  $R$  and  $R'$ .

that  $R'$  is increasing from 0.6 to 0.7 close to the nucleation onset and reaches almost 1 at  $-1.93$  V. The potential dependence of  $\theta$ -scans showed similar trends (not shown).

### 3.6. Influence of the steps on $\theta$ -scans

Fig. 12 plots for different  $\Phi$ -angles the  $\theta$ -scans of a 9–10 ML gold deposit on Si-0.2° ( $U = -1.68$  V). Clearly  $\theta_{\text{Au}(111)}$  oscillates with a periodicity of  $360^\circ$  (Fig. 12a). The amplitude of oscillations ( $0.3^\circ$ ) corresponds to the tilt angle between the Au(111) planes and the *optical plane* of the sample surface. The same experiment around  $\theta_{\text{Si}(111)}$  on Si-0.2° (not shown) gives an amplitude of oscillation  $0.2^\circ$  equal to the miscut angle of this substrate [30,26]. The surprise, however, is that the oscillations of  $\theta_{\text{Au}(111)}$  and  $\theta_{\text{Si}(111)}$  are *out of phase*, which means that the tilt angle  $\theta_{\text{Au-Si}}$ , between the Au(111) and the Si(111) planes, is equal to the *sum* of the two amplitudes. Hence  $\theta_{\text{Au-Si}} = 0.2 + 0.3 = 0.5^\circ$  for the considered deposit. Fig. 12b plots  $\theta_{\text{Au-Si}}$  as a function of the deposition potential. On Si-0.2°,  $\theta_{\text{Au-Si}}$  is essentially constant and equal to  $0.4^\circ$ . On Si-2°,  $\theta_{\text{Au-Si}}$  decreases continuously with increasing  $\eta$  from  $2^\circ$  to close to  $0^\circ$ . Last, Fig. 12c is showing

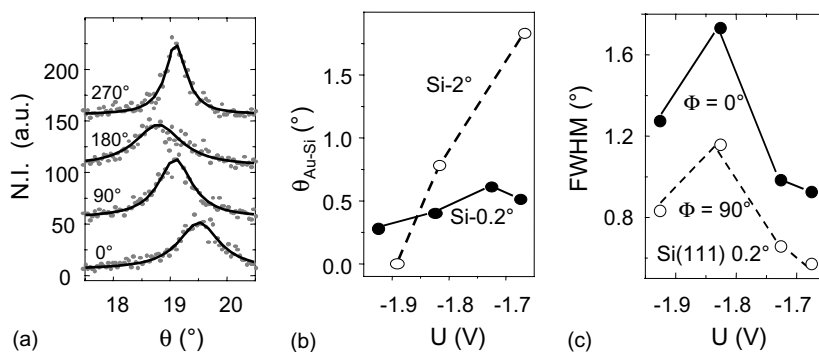


Fig. 12. (a)  $\theta$ -scans around  $\theta_{\text{Au}(111)}$  recorded for different  $\Phi$  angles. (b) Variation of  $\theta_{\text{Au-Si}}$  as a function of the deposition potential for two miscut angles. (c) Variations of the peak linewidth as a function of the deposition potential. Open symbols refer to  $\Phi = 90^\circ$  and bold symbols to  $\Phi = 0^\circ$ . Note that the FWHM is smaller for  $\Phi = 90^\circ$ .

that, at any deposition potential, the peak linewidth of  $\theta$ -scans is significantly smaller with the beam *parallel* to steps (open symbols) than with the beam *perpendicular* to them (closed circles). This is suggesting that the steps have some influence on the orientation of the gold islands.

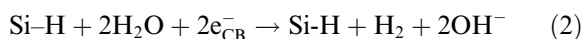
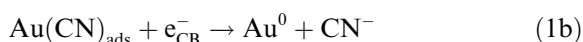
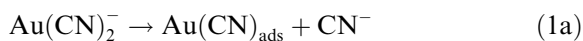
#### 4. Discussion

Gold electrodeposition leads to a Volmer–Weber growth on H-Si(111) likewise gold evaporation on the same surface [31]. In agreement with Oskam and Searson [15], we find that the nucleation is progressive as indicated by the dimensionless transients in Fig. 4c and the wide size distribution of the gold islands imaged by AFM (Figs. 5–7). The observation of a constant density of islands by AFM (Fig. 5a–c) is not contradictory because the images corresponds to deposition times greater than  $t_{\text{max}}$  (the nucleation stops for  $t \sim t_{\text{max}}$ ). In the studied range of potential, AFM shows that the 3D nm-sized islands *exclusively* decorate the terrace edges (Figs. 5–7). The improvement of the (111) texture (Fig. 8) and epitaxy (Fig. 9) upon growth is attributed to the slower growth rate of the Au(111) planes with respect to the other orientations. It is a general rule that the slower growth planes are dense planes and that they impose the film texture upon growth. The sixfold symmetry of the  $\Phi$ -scans (Figs. 9 and 10) indicates epitaxy with the silicon (111) surface.

Part of the clusters are in epitaxy with *bulk* silicon, according to the relationship  $\text{Au}(111)[1\bar{1}0]||\text{Si}(111)[1\bar{1}0]$ , while the remaining ones are rotated by  $180^\circ$ . The epitaxy may be explained by the atomic model displayed in Fig. 13 where a *relaxed* (111) gold monolayer placed onto a  $1 \times 1$ -Si(111) surface builds the commensurate  $3 \times 3$  structure [ $3 \times (\text{Si-Si} = 3.84 \text{ \AA}) = 4 \times (\text{Au-Au} = 2.88 \text{ \AA}) = 11.52 \text{ \AA}$ ].<sup>3</sup> From this model we conclude that the edges of polyhedron islands are gold densely packed directions.

##### 4.1. Specificity of the silicon–electrolyte electrochemical interface

Unlike metal evaporation, metal electrodeposition on silicon involves the donation of conduction band electrons to reduce the metal complexes to metallic atom. In the case of gold electrodeposition we may consider the following reactions:



<sup>3</sup> The  $(7 \times 7)\text{R}19^\circ 1$  is another commensurate structure. It accounts for the satellites peaks shifted by  $\pm 19^\circ$  with respect to main peaks (Fig. 10b). These were not discussed because of their low intensity. Clusters rotated by  $\sim 20^\circ$  with respect to the main axis are also occasionally found by AFM (see Fig. 7).

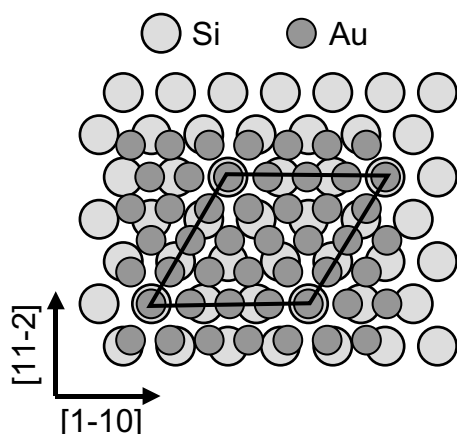


Fig. 13. Atomic model of the Au–Si interface accounting for the observed relation of epitaxy. Only the silicon atoms of the topmost surface plane are displayed.

Reaction (1) is the reduction of the gold cyanide complexes in a two-step process as proposed by Oskam and Searson [14]. In the first step (reaction (1a)), the gold complex is partially dissociated and adsorbed on the surface as  $\text{Au}(\text{CN})_{\text{ads}}$ . It is reduced to metallic gold in the second step by capture of one conduction band electron (reaction (1b)). Reaction Eq. (2) is the decomposition of water into molecular hydrogen. On the molecular level [32] this reaction involves the desorption of one hydrogen atom from the silicon surface in order to build the molecule of  $\text{H}_2$ . Hence, reaction Eq. (2) transiently generates dangling bonds on the surface. The rate of reactions (1) and (2), averaged over the entire surface, increases with  $\eta$ . From the curve in inset of Fig. 3, the contribution of reaction (2) to the deposition current becomes significant for  $U < -1.8$  V while it may be neglected closer to the nucleation onset.

One specificity of the electrochemical electron transfer is that its rate may be highly site dependent on the atomic scale. A striking example of the influence of the surface structure on electrochemical transfer is the reaction of chemical etching of silicon, which is totally *anisotropic* and exclusively occurs at the silicon step edges because the hydrolysis of Si–H bonds into silanol groups is much faster on such sites [32]. In analogy with the etching reaction, we infer that reaction (2) is also

much faster at steps than on terraces because the splitting of Si–H bonds is more favorable at step sites for energetic and conformation reasons (Fig. 1b). As the rate of reaction (2) increases with  $\eta$ , the density of step dangling bonds also increases with  $\eta$ . In the same way reaction 1b is faster at step sites because the gold atoms increase their coordination number with the silicon lattice. The adsorption stage (reaction (1a)) is, at reverse, thought to be nearly site independent.

#### 4.2. Origin of the exclusive gold nucleation at steps

As evidenced by AFM observations (Figs. 5d and 7b–c) the nucleation of the gold film is *not homogeneous* and occurs *exclusively* at the terrace edges for  $-1.92$  V  $< U < -1.60$  V. At small  $\eta$ , a preferential nucleation at steps is not a surprise because steps are usually favorable sites. It is the total absence of nucleation on the (1 1 1) terraces, at larger  $\eta$  which constitutes a strong surprise because the flux seems sufficiently large to allow the formation of critical nuclei on atomically smooth H–Si(1 1 1) terraces (the average flux is  $\sim 2$  ML/s for 10–15 ML deposited in 7 s). In the case of indium evaporation, STM observations show that islands nucleate on H–Si(1 1 1) terraces for much smaller fluxes ( $< 0.1$  ML/s) [34].

According to the mean field nucleation theory, the density  $n_x$  of islands varies as  $(D/F)^{-\chi}$  on defect free surfaces (i.e. on flat terraces).  $F$  denotes the deposition flux and  $D$  is the diffusion coefficient of adatoms on the surface. The scaling exponent  $\chi$  is depending on the size of the critical nuclei [33]. This law is general. The conditions of flux and temperature to reach a given  $n_x$  are nevertheless depending on the system though  $D$  and  $\chi$ . Using Brune's [33] plots of  $n_x$  as a function of  $(D/F)$ , we estimate, in the case of indium evaporation, that  $(D/F) \sim 10^8$  to account for the observed  $n_x \sim 10^{11}$  islands/cm<sup>2</sup> [34]. This corresponds to a quite large diffusion coefficient ( $F = 0.01$  to  $0.1$  ML/s) in agreement with calculation showing that metal adatoms diffuse much faster on H–Si(1 1 1) than on clean  $7 \times 7$  surfaces [35]. This is because the saturation of dangling bonds with H atoms removes all electronic states [36] and promotes a very shallow electronic corrugation ( $< 0.2$  Å in STM images

[37]). In our case, the absence of islands on terraces as wide as 100 nm implies that  $(D/F) \gg 10^8$  [33]. Accounting for the difference of fluxes between the two experiments ( $F \sim 2$  ML/s in this work), we conclude that the diffusion coefficient of Au is several orders of magnitude larger at the solid–electrolyte interface than that of indium in vacuum. Such an enhanced diffusion is consistent with reaction (1a) because halides and  $\text{CN}^-$  anions increase the surface mobility of gold adatoms on Au surfaces [38]. This effect is amplified here because the H-monolayer reduces the interactions between the adsorbates  $\text{Au}(\text{CN})_{\text{ads}}$  and the silicon.

An enhanced surface diffusion is nevertheless not sufficient to explain the absence of gold clusters on H–Si(111) terraces. The presence of the cyanide complexing agents in solution requires the generation of Si–Au bonds to stabilize a critical nucleus on the surface. This is the second prerequisite. Because the step sites are the most favorable desorption sites of hydrogen, the *first* gold adatoms will preferentially form a stable nucleus at steps where the formation of Si–Au bonds ensure that the Au atoms are not re-dissolved. Such a mechanism, where the metal atoms is deposited at the silicon dangling bonds, was assumed for nickel electroless deposition from a  $\text{NiSO}_4\text{--NH}_4\text{F}$  solution because no Ni deposition occurs if the silicon is not etched at a sufficient rate [25]. In this case the silicon dangling bonds are generated by the chemical etching reaction [32]. The same mechanism explains that electroless deposition from a diluted  $\text{CuSO}_4\text{--NH}_4\text{F}$  [22] leads to small Cu clusters which decorate the steps (the steps are the stage of preferential etching).

#### 4.3. Growth mechanism

The main experimental fact is the improved epitaxy with increasing  $\eta$ ,  $\theta$  and  $\Phi$ -scans (Figs. 10 and 11) indicate indeed that the film structure is rather powder-like, close to the nucleation onset (–1.6 V), with 40% grains having no preferential orientations ( $R \simeq 0.6$ ). Such films are imaged with difficulty since the AFM tip easily wipes the islands. As soon as  $U < -1.7$  V a well defined epitaxy with a (111) orientation is established. For

the same metal thickness,  $R$  reaches 90% at –1.92 V against only 60% at –1.6 V (Fig. 11c). Accordingly the gold islands present a much better-defined polyhedron shape in AFM images (Fig. 7). Such islands are also strongly attached to the surface (they are not wiped by the AFM tip).

After the formation of a stable nucleus at steps (Fig. 14a), the growth may proceed on terraces from such preferential nucleation centers, because they become soon the stage of the electron transfer and also because they act as sink for diffusing Au atoms. A priori, a good epitaxy with the (111) terraces implies sufficiently strong interactions with the substrate. Clean Si(111) favors metal epitaxy [4] whereas H-terminated Si(111) does not because the saturation of Si dangling bonds with H atoms prevents the formation of a stable chemical bond between the metal and the silicon. Therefore the observed epitaxy of Au electrodeposits suggests that an intimate Au–Si contact can also be formed on terraces. The following growth mechanism is tentatively proposed after formation of the precursor nucleus (Fig. 14a). At large overpotential, the island is in *direct* contact with the silicon (Fig. 14b). The H-layer is progressively unzipped from the boundary between the H-layer and the gold step because reaction (2) is catalyzed there and the rate of H-desorption greatly amplified. We stress that the rate of *spontaneous* H-desorption on naked H–Si(111) terraces is extremely small. The growth remains 2D as long as the removal rate of H atoms is sufficiently large to allow the incorporation of all incoming gold adatoms. Very soon 3D growth occurs however due to gold on gold deposition (electrons are transferred from the deposited clusters). The crossover between the 2D and 3D growth regimes is determined by the size and the surface density of the metal nuclei [42]. Close to the onset of nucleation the rate of reaction (2) is negligible on the gold islands. As a result the Au adatoms stick to the nucleus on the step and the islands grow *atop* the H-layer (Fig. 14d). This scenario correlates very well with the observation that films grown close to –1.6 V are weakly interacting with the substrate (islands are wiped by the AFM tip). At intermediate potentials, a mixed structure such as the one sketched in Fig. 14c might be obtained.

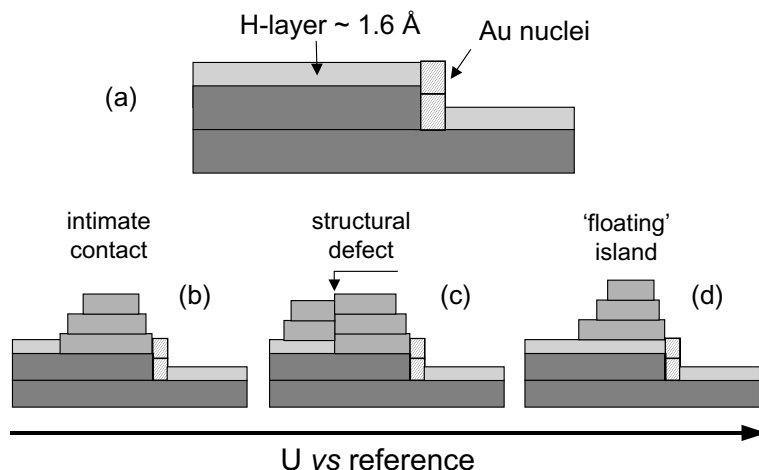


Fig. 14. Qualitative model explaining the correlation between the quality of the epitaxy and the deposition potential. (a) Nucleation stage: a stable nucleus is formed at the step where preferential desorption of the hydrogen takes place. This nucleus acts as precursor for the lateral growth on the terrace. (b)–(d) Growth model as a function of the deposition potential: at large overpotential (b) the H-termination is removed by local H-desorption from the boundary between the H-layer and the gold monolayer. An intimate Si–Au contact is built. Close to the nucleation onset (d) the gold island is growing atop the H layer. Such islands are wiped by the AFM tips. At intermediate potentials (c), the Au island is only partly in contact with the silicon surface.

Gold evaporation, which constitutes an intermediate case in the scale of reactivity with silicon [39], promotes a partial removal of the H-layer upon evaporation on H–Si(111) [31]. Fig. 14 evidences therefore a major difference between the two methods of deposition. At the electrochemical interface, the removal of the H-monolayer is monitored by the catalytic properties of the deposit towards reaction (2). Depending on the potential, the deposit may be in intimate contact with silicon or may float above the H-monolayer. The result seems not dependent on the reactivity of gold with respect to silicon, whereas, in vacuum, the removal of H atoms is depending, to a large extent, on the metal reactivity. In the case of indium, a weakly reacting metal, the H-layer is thought to remain intact under the deposit because the Si–In bond energy (2.5–2.8 eV) is much smaller than the Si–H bond energy ( $\sim 3.5$  eV) [34]. In the case of very reactive metals (e.g. Ni, Fe, Cu) the first 2 ML are embedded under the surface plane and the H-monolayer remains *intact* (case of Fe and Ni [40,41]). Above 2 ML the H layer is destroyed and silicide formation is anticipated. Metal electrodeposition enables the formation of a direct contact without silicide formation.

#### 4.4. Origin of the rotation of gold nanocrystals

The  $\Phi$ -scans (Figs. 9 and 10) exhibit a sixfold symmetry reflecting the symmetry of the silicon surface and not the threefold symmetry of the bulk. One could attribute this observation to stacking faults but it is unrealistic to attain 50% of stacking faults at  $-1.93$  V. The above sixfold symmetry rather indicates that the (111) gold nanocrystallites take two possible orientations, which are rotated by  $180^\circ$  from each other. The same observation has been reported upon silver evaporation [43]. We believe that our observations stem from a different reason, principally because the nucleation occurs exclusively at steps, which is not the case in the UHV.

The starting point of the discussion is the co-existence of triangles of type (A) and (B) in Fig. 7 which preferentially overlap with the upper and the bottom terrace. Their edges correspond to densely packed directions of fcc gold and XRD suggests that the facets are (111) like facets. These are also energetically favorable. Therefore, we propose an atomistic model in which the lateral growth of islands on terraces starts with the formation of the smallest possible pyramidal island

with a triangular (111) base and (111) facets. Such an island is represented in Fig. 15. Its triangular base corresponds to one half of the  $3 \times 3$  unit cell shown in Fig. 13 with one edge parallel to the step to conform to Fig. 7. The tip of the triangle is therefore either pointing towards the upper (Fig. 15a) or on the bottom (Fig. 15b) terrace. Adding subsequent atomic planes according to the fcc stacking ABC creates two Au(111) nanocrystals, which bulk axis are rotated by  $180^\circ$  with respect to each other. On the upper terrace the axis of the cluster are parallel to those of the silicon crystal (Fig. 15a). Within the frame of this growth model, two effects might be responsible for the experimental increase of  $R'$  with  $\eta$ . The first one is a reduction of the Schwoebel effect [44] at large  $\eta$ , because the accumulation of electrons at the silicon surface likely smoothes out the diffusion barrier across the steps. The second one is the potential dependence of the structure of nucleation sites. The desorption of H atoms occurs indeed at different potentials on kink sites and step monohydrides.

As the triangles of type (A) are overlapping with the upper terrace (Fig. 7), we conclude from the

above model that they are in epitaxy with the silicon, according to the relationship  $\text{Au}(111)\text{--}[1\bar{1}0] \parallel \text{Si}(111)\text{--}[1\bar{1}0]$ , and that they account for the *even* peaks in  $\Phi$ -scans. As a consequence, the triangles of type (B) account for the *odd* peaks in  $\Phi$ -scans because they are rotated by  $180^\circ$ . Within this model, the ratio  $R'$  should be equal to the ratio [volume of triangular islands of type (B)/volume of triangular islands of type (A)]. We attempted to verify this from the AFM image in Fig. 7 by counting the population of the different islands. The ratio of triangles of type (A) to triangles of type (B) is 5:1. Examination of the non-triangular islands shows that 50% of the islands are overlapping preferentially with the upper terrace at  $U = -1.73$  V, whereas only 10% overlap with the lower terrace. The center of gravity of the remaining islands (40% of the total) overlap equally with both the upper and bottom terrace. From this analysis one finds  $R' \sim 0.33$ , which is smaller than the value 0.65 derived from the corresponding  $\Phi$ -scan. The principal cause for this discrepancy comes from the fact that we could not consider the volume of islands in our estimate. It was also impossible to make such a detailed analysis at more

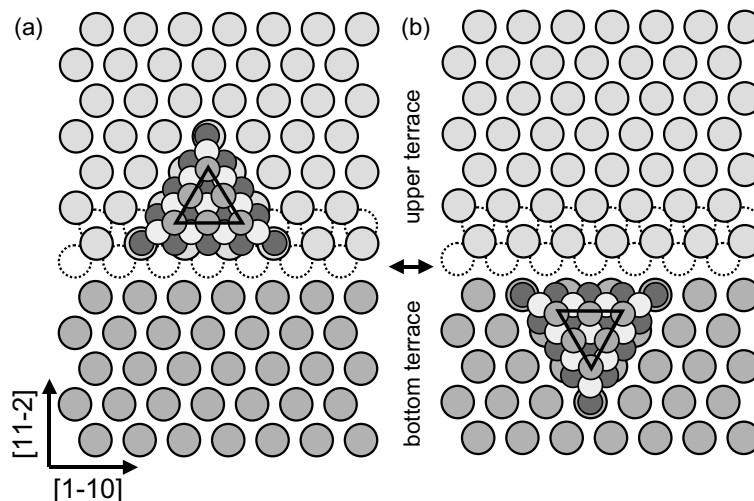


Fig. 15. Atomic model accounting for the coexistence of epitaxial gold crystals rotated by  $180^\circ$  on the Si(111) surface. After nucleation of the precursor nucleus, a half  $3 \times 3$  unit cell is first formed on the Si(111) plane. Adding the second and third atomic planes builds a pyramidal cluster with (111) facets. The cluster on upper terrace (a) is in epitaxy with Si(111) according to the relationship  $\text{Au}(111)\text{--}[1\bar{1}0] \parallel \text{Si}(111)\text{--}[1\bar{1}0]$ . It corresponds to triangles of type (A) in AFM images. The cluster on the bottom terrace (b) is rotated by  $180^\circ$  and corresponds to triangles of type (B). The precursor nucleus defined in Fig. 14a is not represented.

negative potentials of deposition because the larger island density hampers the precise localization of the silicon steps.

#### 4.5. Influence of the step density on $\theta_{\text{Au-Si}}$

The influence of steps on the orientation of the gold islands is clearly evidenced by Fig. 12. On Si-0.2°,  $\theta_{\text{Au-Si}}$  is essentially potential independent. In this case, simple geometrical considerations may explain the tilt angle of 0.4° because the islands size is always smaller than twice the terrace width (Fig. 16a). The mismatch between the height of a gold monolayer (2.35 Å) and that of a silicon step (3.14 Å) makes that the gold plane overlapping with both terraces does not sit properly on either of the two terraces. For a 50 nm wide island, the tilt angle is  $\theta_{\text{Au-Si}} \sim \arctg [(0.314 - 0.235)/(25)] = 0.18^\circ$ , which is fairly close to the experimental value in Fig. 12b. On Si-2°, the stronger effect of the potential on  $\theta_{\text{Au-Si}}$  arises from the fact that the island size varies in greater proportion. And may be close or bigger than twice the terrace width ( $W = 10$  nm). At  $U \sim -1.75$  V the islands are 50 nm wide and overlap with several terraces (Fig.

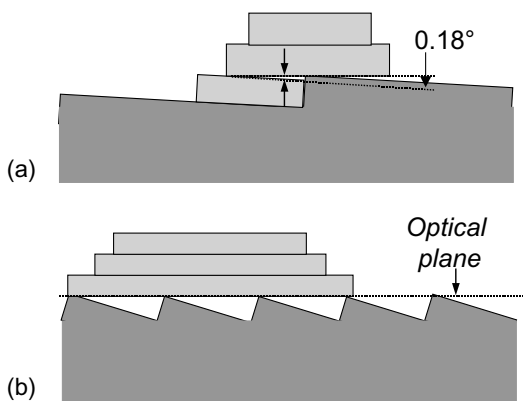


Fig. 16. Schematic explanation for the tilt angle  $\theta_{\text{Au-Si}}$  between the Au(111) and Si(111) planes. (a) When the island is smaller than the terrace width, the mismatch between the height of a gold monolayer and the silicon step induces a small tilt of the second gold atomic plane deposited across the step. (b) When the islands are wider than two terraces, they are deposited across several steps. The gold Au(111) planes are parallel to the optical plane and  $\theta_{\text{Au-Si}}$  is equal to the miscut angle of the substrate.

16b). The Au(111) planes are parallel to the optical plane of the sample surface and  $\theta_{\text{Au-Si}}$  is equal to the miscut angle of the substrate, in good agreement with Fig. 12b. At -1.92 V, the island size become smaller than the width of two terraces ( $\sim 20$  nm).<sup>4</sup> They sit as shown in Fig. 16a, with the Au(111) planes practically parallel to Si(111) planes, which reduces  $\theta_{\text{Au-Si}}$ .

The second effect of the step is a broadening of the linewidth of  $\theta$ -scans when the X-ray beam is perpendicular to the step direction. This difference can be simply rationalized by considering that the Si step induces structural defects in the direction perpendicular to it if the Au island is positioned across it. The step is adding a degree of freedom to accommodate the gold lattice on the silicon lattice. In Fig. 7, 40% of islands adopt such a position. The fluctuations of orientations are less significant parallel to the steps because of the absence of such surface defects. For the remaining grains, which are preferentially overlapping with the upper terraces, this effect should be less important.

## 5. Conclusion

In conclusion we have shown that the electrochemical growth of Au on structurally well-defined vicinal H-terminated Si(111) surfaces occurs by selective nucleation of 3D nm-sized gold islands at the silicon steps. The potential of deposition controls both the density of islands along the steps and the film structure. Under optimum conditions, i.e. at sufficiently negative potential, a nearly perfect replication of the stepped surface structure is obtained with epitaxial nm-sized islands decorating the silicon steps. All observations are consistent with the proposed reaction scheme and growth model. In initial stages, a stable critical nucleus is first formed on the dangling bonds generated at steps by the decomposition of water.

<sup>4</sup> A precise measure of the island size is difficult on Si-2° because the tip is not sufficiently sharp. The surface density of islands being 10 times greater on Si-2°, we may estimate, for an equivalent metal thickness, that the islands are smaller by a factor  $\sim 10^{1/3} = 2.15$  on Si-2° than on Si-0.2°.

This nucleus acts soon as preferential nucleation center for the lateral growth on terraces. During this phase, and at sufficiently negative potential, the H-layer is progressively removed from the surface within a catalytic process occurring at the Au/H–Si interface, while the H-termination remains intact between the metal islands. Close to the nucleation onset, the H-layer remains intact under the deposit and the film has a rather powder-like structure.

### Acknowledgements

M.L. Munford gratefully acknowledges CAPES (Brazil) for a Ph.D. fellowship during his stay in France and the “Direction des Affaires Internationales” (Université P & M Curie) for a complementary financial support. We also thank M.-C. Bernard for the RBS measurements. We also acknowledge Siltronix (France) for preparing the substrates according to our specifications.

### References

- [1] T. Ogino, H. Hibino, Y. Homma, Y. Kkobayashi, K. Prabhakaran, K. Sumitomo, H. Omi, *Acc. Chem. Res.* 32 (1999) 447.
- [2] A. Kirakosian, J.L. Lin, D.Y. Petrovykh, J.N. Crain, F.J. Himpsel, *J. Appl. Phys.* 90 (2001) 3286.
- [3] F.J. Himpsel, A. Kirakosian, J.N. Crain, J.L. Lin, D.Y. Petrovykh, *Solid State Commun.* 117 (2001) 149.
- [4] K. Oura, V.G. Lifshits, A.A. Saranin, A.V. Zotov, M. Katayama, *Surf. Sci. Report* 35 (1999) 1.
- [5] P. Jakob, Y.J. Chabal, *J. Chem. Phys.* 95 (1991) 2897.
- [6] P.M. Hoffmann, A. Radisic, P.C. Searson, *J. Electrochem. Soc.* 147 (2000) 2576.
- [7] J.C. Ziegler, A. Reitzle, O. Bunk, J. Zegenhagen, D.M. Kolb, *Electrochim. Acta* 45 (2000) 4599.
- [8] T. Zambelli, M.L. Munford, F. Pillier, M.C. Bernard, P. Allongue, *J. Electrochem. Soc.* 148 (2001) C614.
- [9] C. Ji, G. Oskam, P.C. Searson, *Surf. Sci.* 492 (2001) 115.
- [10] B. Rashkova, B. Guel, R.T. Pötzschke, G. Staikov, W. Lorenz, *Electrochim. Acta* 43 (2000) 3021.
- [11] J.C. Ziegler, R.I. Wielgosz, D.M. Kolb, *Electrochim. Acta* 45 (1999) 827.
- [12] J.C. Ziegler, G. Scherb, O. Bunk, A. Kazimirov, L.X. Cao, D.M. Kolb, R.L. Johnson, J. Zegenhagen, *Surf. Sci.* 452 (2000) 150.
- [13] G. Oskam, J.G. Long, A. Natarajan, P. Searson, *J. Phys. D: Appl. Phys.* 31 (1998) 1927.
- [14] G. Oskam, P. Searson, *Surf. Sci.* 446 (2000) 103.
- [15] G. Oskam, P. Searson, *J. Electrochem. Soc.* 147 (2000) 2199.
- [16] A.P. O’Keeffe, O.I. Kasyutich, W. Schwarzacher, L.S. de Olivera, A.A. Pasa, *Appl. Phys. Lett.* 73 (1998) 1002.
- [17] K. Attenborough, H. Boeve, J. De Boeck, G. Borghs, J.P. Celis, *Appl. Phys. Lett.* 74 (1999) 2206.
- [18] L. Seligman, M.L. Sartorelli, A.A. Pasa, W. Schwarzacher, O.I. Kasyutich, *J. Magn. Magn. Mater.* 226–230 (2001) 752.
- [19] M.L. Munford, L. Seligman, M.L. Sartorelli, E. Voltolini, L.F.O. Martins, W. Schwarzacher, A.A. Pasa, *J. Magn. Magn. Mater.* 226–230 (2001) 1613.
- [20] F. Maroun, F. Ozanam, J.N. Chazalviel, W. Teiss, *Vibrational Spec.* 19 (1999) 193.
- [21] F. Ronkel, J.W. Schultze, R. Arens-Fischer, *Thin Solid Films* 276 (1996) 40.
- [22] T. Homma, C.P. Wade, C.E.D. Chidsey, *J. Phys. Chem.* 41 (102) 7919.
- [23] S. Warren, A. Reitzle, A. Kazimirov, J.C. Ziegler, O. Bunk, L.X. Cao, F.U. Renner, D.M. Kolb, M.J. Bedzyk, J. Zegenhagen, *Surf. Sci.* 496 (2002) 287.
- [24] P. Gorostiza, R. diaz, J. Servat, F. Sanz, J.R. Morante, *J. Electrochem. Soc.* 144 (1997) 909.
- [25] P. Gorostiza, M. Kulandainathan, R. Diaz, F. Sanz, P. Allongue, J.R. Morantes, *J. Electrochem. Soc.* 147 (2000) 1026.
- [26] M.L. Munford, R. Cortes, P. Allongue, *Sensors Mater.* 13 (2001) 259–269.
- [27] C.P. Wade, C.E.D. Chidsey, *Appl. Phys. Lett.* 71 (1997) 1679.
- [28] H. Fukidome, M. Matsumura, *Appl. Surf. Sci.* 130 (1998) 146.
- [29] P. Allongue, C. Henry de Villeneuve, S. Morin, R. Boukherroub, D.D.M. Wayner, *Electrochim. Acta* 45 (2000) 4591.
- [30] M.L. Munford, Ph.D. Thesis, Université Paris 6 in Paris (France) and UFSC in Florianopolis (Brazil), 2002.
- [31] C. Grupp, A. Taleb-Ibrahimi, *Phys. Rev. B* 57 (1998) 6258.
- [32] P. Allongue, V. Costa-Kieling, H. Gerischer, *J. Electrochem. Soc.* 143 (1993) 1018; P. Allongue, V. Costa-Kieling, H. Gerischer, *Electrochim. Acta* 40 (1995) 1353.
- [33] H. Brune, *Surf. Sci. Report* 31 (1998) 125; H. Brune, G.S. Bales, J. Jacobsen, C. Boragno, K. Kern, *Phys. Rev. B* 60 (1999) 5991.
- [34] F.P. Leisenberger, H. Ofner, M.G. Ramsey, F.P. Netzer, *Surf. Sci.* 383 (1997) 25.
- [35] N. Enomoto, T. Hoshino, M. Hata, M. Tsuda, *Appl. Surf. Sci.* 130–132 (1998) 237.
- [36] D.M. Kolb, *Prog. Surf. Sci.* 51 (1996) 109; *Electrochim. Acta*, 45 (2000) 2387.
- [37] P. Allongue, *Phys. Rev. Lett.* 77 (1996) 1986–1989.
- [38] S. Gallego, J. Avila, M. Martin, X. Blasé, A. Taleb, P. Dumas, M.C. Asencio, *Phys. Rev. B* 61 (2000) 12628.
- [39] J.A. Kerr, in: D.R. Lide (Ed.), *CRC Handbook of Chemistry and Physics 1999–2000: A Ready-Reference Book of*

- Chemical and Physical Data (CRC Handbook of Chemistry and Physics), 81st ed., CRC Press, Boca Raton, Florida, USA, 2000.
- [40] M.G. Martin, J. Avila, M. Gruyters, C. Teodorescu, P. Dumas, Y.J. Chabal, M.C. Asencio, *Appl. Surf. Sci.* 123–124 (1998) 156.
- [41] K. Hirose, A. Hanta, M. Uda, *Appl. Surf. Sci.* 162–163 (2000) 25.
- [42] P. Allongue, *Modern Aspects of Electrochemistry*, B.E. Conway (Ed.), Plenum Press, New York, Chapter 4, vol. 23, 1992, p. 239.
- [43] K. Sumitomo, T. Kobayashi, F. Shoji, K. Oura, *Phys. Rev. Lett.* 66 (1991) 1193.
- [44] R.L. Schwoebel, E.J. Chipsey, *J. Appl. Phys.* 37 (1966) 3682;  
R.L. Schwoebel, *J. Appl. Phys.* 40 (1969) 614.